



# Z-scheme g-C<sub>3</sub>N<sub>4</sub>@Cs<sub>x</sub>WO<sub>3</sub> heterostructure as smart window coating for UV isolating, Vis penetrating, NIR shielding and full spectrum photocatalytic decomposing VOCs

Yuan Li<sup>a</sup>, Xiaoyong Wu<sup>a,\*</sup>, Jun Li<sup>a</sup>, Kai Wang<sup>a</sup>, Gaoke Zhang<sup>a,b,\*\*</sup>

<sup>a</sup> Hubei Key Laboratory of Mineral Resources Processing and Environment, Hubei Provincial Collaborative Innovation Center for High Efficient Utilization of Vanadium Resources, School of Resources and Environmental Engineering, Wuhan University of Technology, 122 Luoshi Road, Wuhan 430070, China

<sup>b</sup> State Key Laboratory of Silicate Materials for Architectures, Wuhan University of Technology, Wuhan 430070, China

## ARTICLE INFO

### Keywords:

Smart window coating  
Z-scheme heterostructure  
Small polaron hopping  
Nanowires (NW) cesium tungsten bronze  
g-C<sub>3</sub>N<sub>4</sub>

## ABSTRACT

Multifunctional smart window coating is expected for indoor decontaminating and energy-saving, because of the highly desired for comfortable and green quality of indoor conditions. However, normal smart window coating only absorbs UV and NIR light to transform them into heat energy without maximum exploitation of solar energy. Herein, a series of unique g-C<sub>3</sub>N<sub>4</sub>@Cs<sub>x</sub>WO<sub>3</sub> nanocomposites are prepared via ultrasonic assisted strategy, exhibiting great ultraviolet (UV) isolating, visible light (Vis) penetrating and near-infrared (NIR) heat-shielding features which is superior over that of tin-doped indium oxide (ITO). More importantly, these composites display excellent VOCs (HCHO or/and toluene) decomposing properties under the full spectrum of UV, visible and NIR lights irradiation. In this case, the shielded NIR light by composites is further utilized instead of wasting as heat. On the other hand, deep analysis revealed that the high efficiency of photocatalytic decomposing of VOCs by g-C<sub>3</sub>N<sub>4</sub>@Cs<sub>x</sub>WO<sub>3</sub> nanocomposites depends on two sides: firstly, g-C<sub>3</sub>N<sub>4</sub>@Cs<sub>x</sub>WO<sub>3</sub> constructs a nice Z-scheme structure to promote the separation of charge carriers and then enhance photocatalytic oxidation (PCO) effectively; secondly, the small polaron can jump from localized states (LS) to conduction band (CB) of Cs<sub>x</sub>WO<sub>3</sub> under irradiation of NIR (730 nm–1100 nm) and result in a NIR-catalytic reduction. This work provides some indications into the fabrication of the energy-conservation and depollution catalysts as smart window coating with excellent optical characterization and photocatalysis performance.

## 1. Introduction

For the better promotion of living standards, we urgently require both of harmless and comfortable indoor conditions include houses, offices (workplaces) and cars. Firstly, in human health terms, indoor air quality is the most importance because people often spend 90% of life time indoor. As the most important index of indoor air quality, the volatile organic compounds (VOCs), which mainly come from decoration and furniture, significantly deteriorate living standard and seriously effect human health [1,2]. Accordingly, it is very essential to develop a material for VOCs removal. Secondly, in the case of comfortable surroundings, top of the list is a comfortable indoor temperature. However, more than 10% electricity energy has been consumed, typically for air conditioners and fans, to keep a comfortable indoor temperature [3], meanwhile, corresponding amount of CO<sub>2</sub> has been

discharged from power plants. As we know, the main thermal energy source of indoor is the NIR spectrum (780–2500 nm). Therefore, the NIR isolating material which can alleviate the indoor temperature increment in the summer and block the energy loss from warm indoor in the chilly winter, is desirable in the green building field. So, under the consideration of depollution, energy-conservation and less CO<sub>2</sub> emission, the development of some new multifunctional materials for NIR isolating and VOCs photo-decomposing, simultaneously, are promising and strongly required [4].

For this purpose, some corresponding materials, such as tin-doped indium oxide (ITO) [5–7], vanadium dioxide [8–11], lanthanum hexaboride (LaB<sub>6</sub>) [12–14] and hexagonal tungsten bronze (HTB) [15–17], etc., have been proposed. Among them, nanowires (NW) cesium tungsten bronze (Cs<sub>x</sub>WO<sub>3</sub>) displayed great promising application for smart window coating due to the highest Vis penetrating and the strongest

\* Corresponding author at: Hubei Key Laboratory of Mineral Resources Processing and Environment, Hubei Provincial Collaborative Innovation Center for High Efficient Utilization of Vanadium Resources, School of Resources and Environmental Engineering, Wuhan University of Technology, 122 Luoshi Road, Wuhan 430070, China.

\*\* Corresponding author.

E-mail addresses: [parawu521@163.com](mailto:parawu521@163.com) (X. Wu), [gkzhang@whut.edu.cn](mailto:gkzhang@whut.edu.cn) (G. Zhang).

<https://doi.org/10.1016/j.apcatb.2018.02.024>

Received 8 November 2017; Received in revised form 16 January 2018; Accepted 11 February 2018

Available online 12 February 2018

0926-3373/ © 2018 Elsevier B.V. All rights reserved.

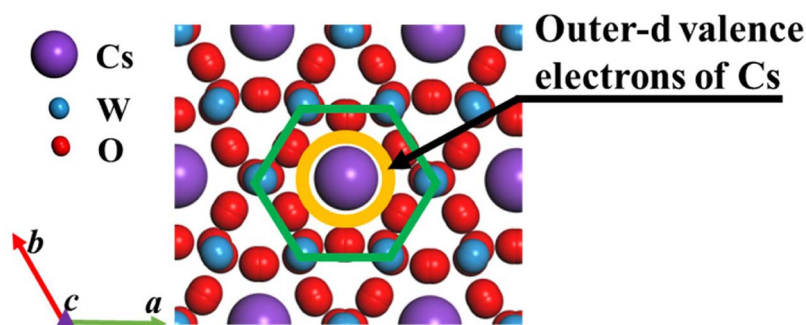


Fig. 1. Polyhedral representation of  $\text{Cs}_x\text{WO}_3$  projected along the c-axis.

NIR shielding among materials as far as we know [18,19]. Recently research revealed that the mechanisms of above properties which are highly correlate to the rich free electrons of  $\text{Cs}_x\text{WO}_3$  (Fig. 1). When  $\text{Cs}_x\text{WO}_3$  was irradiated by the short wavelengths of NIR spectrum (730–1100 nm), the localized electrons (small polarons) either excited to CB or hopped to the neighboring  $\text{W}^{6+}$  site [20–22]. On the other hand, the aggregated free electrons in the CB can induce the localized surface plasma resonance (LSPR) to shield the long wavelengths of NIR spectrum (1100–2500 nm) which approximate to the oscillation frequency of aggregated free electrons [20,23]. Through above mentioned two processes, the majority of NIR light in the solar light could be shielded. However, the absorbed NIR light (accounting for ca. 45% of solar light) by  $\text{Cs}_x\text{WO}_3$  is directly transformed to waste heat without further utilization, which is the common defect for NIR light absorbing materials. Meanwhile, the pure  $\text{Cs}_x\text{WO}_3$  cannot degrade the BTEX (Benzene, Toluene, Ethylbenzene, Xylenes) which are the main compositions of VOCs.

Photocatalysis is a green potential way to decompose VOCs, which is popularly used as one of the above-required multifunction in smart coating. To exhibit high performance of photocatalytic activity, coupling two materials to form heterostructure, especially Z-scheme structure which can enhance the separation of charge carriers and heighten the redox potential [24,25], is feasible and the most effective way to fulfill multifunction. Besides, our earlier studies showed that CB and VB positions of  $\text{Cs}_x\text{WO}_3$  were measured to be ca. 0.69 eV and ca. 3.2 eV, respectively [18], and the CB and VB positions of  $\text{g-C}_3\text{N}_4$  were determined to be ca. -1.01 eV and ca. 1.83 eV [24,25]. In addition, as a kind of non-noble metal catalysts,  $\text{g-C}_3\text{N}_4$  was deemed as one of the most promising candidates, due to their peculiar structure and characteristics, such as being non-noble metal, low cost, thermal and chemical stability, and medium-bandgap indirect semiconductor [26–29]. Accordingly,  $\text{g-C}_3\text{N}_4$  is possible to combine with  $\text{Cs}_x\text{WO}_3$  to synthesize Z-scheme heterostructure [30,31].

In this work, we developed a novel Z-scheme  $\text{g-C}_3\text{N}_4/\text{Cs}_x\text{WO}_3$  nanocomposites as smart coating to achieve the multifunction of UV isolating, Vis penetrating, NIR shielding and VOCs photo-decomposing, simultaneously. In addition, the photocatalytic decomposition of VOCs could be obviously enhanced by this Z-scheme structure as compared to that of pure  $\text{g-C}_3\text{N}_4$ . More importantly, the shielded NIR light by  $\text{Cs}_x\text{WO}_3$  could be further utilized to decompose VOCs instead of wasting as heat. Finally, the detailed mechanisms for photo-decomposing under full spectrum of UV, visible and NIR lights irradiation were discussed.

## 2. Materials and methods

### 2.1. Preparation of catalysts

#### 2.1.1. Preparation of $\text{Cs}_x\text{WO}_3$ nanowires

$\text{Cs}_x\text{WO}_3$  nanowires were synthesized on the basis of water controlled-release process (WCRP) reported previously [32]. All analytical grade reagents purchased from Sinopharm Chemical Reagent Co. Ltd/

Alfa Chemical Reagent Co. Ltd. and used directly without further purification. The synthesized  $\text{Cs}_x\text{WO}_3$  nanowires were reduced in  $\text{H}_2$  (5 vol %)/Ar atmosphere at 550 °C for 1 h to obtain the sapphire cesium tungsten bronze.

#### 2.1.2. Preparation of $\text{g-C}_3\text{N}_4$ nanosheets

Bulk  $\text{C}_3\text{N}_4$  powders were synthesized following the previous paper [33]. Then, 1 g of the yellowish Bulk  $\text{C}_3\text{N}_4$  powders added into 400 ml ethanol mixed solvent (ethanol: deionized water = 3:1) and ultrasonicated for 8 h at room temperature. Next, the ultrasonicated suspension centrifuged at 5000 rpm for 5 min to remove the residual Bulk  $\text{C}_3\text{N}_4$  nanoparticles. Finally, the as-prepared  $\text{g-C}_3\text{N}_4$  nanosheets were dried at 80 °C in a fan oven to obtain slightly yellow powders.

#### 2.1.3. Preparation of $\text{g-C}_3\text{N}_4/\text{Cs}_x\text{WO}_3$ nanocomposites

The certain amounts of pre-synthesized  $\text{g-C}_3\text{N}_4$  nanosheets were re-dispersed via the ultrasonication in 50 ml dehydrated ethanol to obtain the homogeneous suspension. After that, 100 mg  $\text{Cs}_x\text{WO}_3$  nanowires added into the suspension under vigorous stirring for 24 h. Finally, the above suspension was dried in the vacuum oven at 60 °C for overnight to obtain the nanocomposite. The certain amounts of  $\text{g-C}_3\text{N}_4$  additives were 10 mg, 40 mg, 70 mg, 100 mg and 140 mg to combine with fixed amount of  $\text{Cs}_x\text{WO}_3$ , named as 10CNCWO, 40CNCWO, 70CNCWO, 100CNCWO and 140CNCWO, respectively.

#### 2.1.4. Preparation of $\text{g-C}_3\text{N}_4/\text{Cs}_x\text{WO}_3$ nanocomposites coating films

The UV isolating and NIR shielding properties of  $\text{g-C}_3\text{N}_4/\text{Cs}_x\text{WO}_3$  nanocomposites were measured by coating them onto quartz glass substrates (5 cm × 3 cm × 1.2 mm). In a typical film synthesis process, 75 mg sample was dispersed into a mixed solution with 500 mg colloidal and certain amounts of dehydrated ethanol under magnetically stirring for 24 h to obtain a kind of dark blue slurry. After that, the above mixed slurry was forcibly scrolled on the quartz glass substrates. Furthermore, the pure  $\text{Cs}_x\text{WO}_3$ ,  $\text{g-C}_3\text{N}_4$  and ITO (10 Ω) films were prepared under the same conditions for comparison, respectively.

### 2.2. Characterization

The structure and crystallinity of the samples were characterized by X-ray diffraction (XRD) analysis on a D/MAX-RB diffractometer with Cu Kα radiation under the operation conditions of 40 kV and 50 mA. Transmission electron microscopy, high resolution transmission electron microscopy (HRTEM) and selected area electron diffraction (SAED, JEM2100F, 280 kV) were taken to characterize the morphology and microstructure of the products. X-ray photoelectron spectroscopy (VG Multilab2000) was employed to analyze the valence states of the elements with a monochromatic Mg Kα source and a charge neutralizer. The binding energies obtained in the XPS spectral analysis were adjusted for specimen charging by referencing C 1s to 284.5 eV. The transmittance for each composite film was measured on a Lambda 750 S UV/Vis/NIR Spectrometer (PerkinElmer, American). Photoluminescence (PL)

emission spectra were collected by a RF-5301PC spectrofluorometer (Shimadzu, Japan) with emission wavelength of 312 nm. The ESR experiments were recorded by an electron paramagnetic resonance (EPR) spectrometer (A300-10, Bruker) to detect the unpaired electron or singly ionized oxygen vacancies. Gaseous intermediates were analyzed by collecting air samples at the reactor outlet in stainless steel tubes packed with 50 mg Tenax TA. The flow rate was 15 ml/min, and the samples were collected over each 20 min. These adsorption tubes were analyzed using ATD-GC/MS (Turbomatrix 650 ATD, PerkinElmer; GCMS-QP2010, Shimadzu) and GC-FID (GC-2014C, Shimadzu).

### 2.3. Catalytic activity test

The degradation of VOCs (HCHO and toluene) were carried out in a stainless-steel vessel with a quartz glass top. The covered glass Petri dish with 50 mg catalyst was put on the bottom of vessel. 2  $\mu$ l HCHO (38%)/ toluene was injected into the vessel immediately. Then, the VOC (HCHO/ toluene) solution was volatilized completely after heated by the 75 W NIR lamp for 30 min or more. Then, the cover of glass Petri dish was removed to go to the adsorption process until reach adsorption/desorption equilibrium. Each set of experiment was irradiated by 300 W Xe lamp and cooled by water recycle system to make sure the reaction under room temperature (Fig. S1). Furthermore, the concentration of HCHO, toluene, CO<sub>2</sub>, and water vapor were measured by an online Photoacoustic IR Multigas Monitor (INNOVA air Tech Instruments Model 1412). The variable concentration of HCHO, toluene and CO<sub>2</sub> (the difference between target gas concentrations at *t* reaction time and initial time) were investigated to evaluate the catalytic performance.

The removal ratio of HCHO/toluene ( $\eta_{\text{HCHO/toluene}}$ ) was determined as:

$$\eta_{\text{HCHO/toluene}}(=) \frac{C_i - C_t}{C_i}$$

where  $C_i$  (ppm) is the initial equilibrium concentration of HCHO/toluene and  $C_t$  (ppm) is the concentration of HCHO/toluene at the *t* reaction time.

The increase ratio of CO<sub>2</sub> ( $\eta_{\text{CO}_2}$ ) was determined as:

$$\eta_{\text{CO}_2}(=) \frac{C_{t^*} - C_{i^*}}{C_{i^*}}$$

where  $C_{i^*}$  (ppm) is the initial equilibrium concentration of CO<sub>2</sub> and  $C_{t^*}$  (ppm) is the concentration of CO<sub>2</sub> at the *t* reaction time.

## 3. Results and discussion

XRD was used to investigate the phase and crystallographic structure. The insert of Fig. 2 shows the XRD patterns of the nanocomposites with the pure one for each component. The diffraction peaks of 40CNCWO nanocomposites are similar with that of pure Cs<sub>x</sub>WO<sub>3</sub>. Due to the overlaid by the peaks of g-C<sub>3</sub>N<sub>4</sub>, it can be noted that the intensity of characteristic peaks  $2\theta = 23.6^\circ$ ,  $27.9^\circ$  were changed to some extent with the increasing amount of g-C<sub>3</sub>N<sub>4</sub> but without change for the peak positions, indicating the less amount of g-C<sub>3</sub>N<sub>4</sub> has not significant effect on the phase and crystallographic structure of Cs<sub>x</sub>WO<sub>3</sub>, because of the amorphous cloud-like g-C<sub>3</sub>N<sub>4</sub>, and their high dispersion via the assist of ultrasonication and vigorous agitation. In addition, the Raman spectroscopy has been used to detect the existence of g-C<sub>3</sub>N<sub>4</sub> (Fig. S2). Several characteristic peaks of g-C<sub>3</sub>N<sub>4</sub> at 472, 712, 980 and 1226 cm<sup>-1</sup> are observed in the spectra of 40CNCWO [34].

To obtain the microscopic morphology and structure information, the TEM, HRTEM and mapping analysis have been processed to research the formation of hybrid binary composites. The crystal planes and lattice fringes were investigated by the HRTEM. As shown in Fig. 3b, it is easily viewed that the Cs<sub>x</sub>WO<sub>3</sub> possessed a [200] orientation with the 0.32 nm lattice fringe spacing, confirmed by their

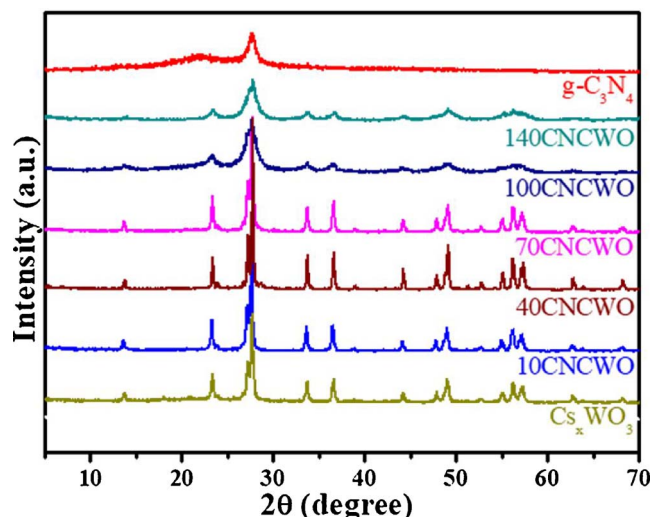


Fig. 2. XRD patterns of nanocomposites with the pure one for each component.

corresponding SAED image in Fig. 3c. All the elements are spatially distributed as confirmed by elemental mapping which is shown in Fig. 3d–i. It is illustrated that the Cs, W and O elements exhibit to rod-like Cs<sub>x</sub>WO<sub>3</sub> and the C and N elements indicate to cloud-like nanosheets C<sub>3</sub>N<sub>4</sub>, respectively. The above results could prove that Cs<sub>x</sub>WO<sub>3</sub> successfully anchored onto the cloud-like g-C<sub>3</sub>N<sub>4</sub> sheets (Fig. 3a).

To further analyze the chemical composition of the as-prepared samples, XPS has been employed in the next process. The insert of Fig. 4a–c shows the high-resolution XPS spectra for W 4f and O 1s profiles of 40CNCWO samples, respectively. W 4f binding-energy (BE) peaks are located at 34.1 eV, 36.5 eV, 35.3 eV, 37.5 eV (Fig. 4b). The above results agree with the reported BE values of W species [35], demonstrating the higher energy peaks 35.4 eV from W 4f7/2 and 37.5 eV from W 4f5/2, are attributed to W<sup>6+</sup> and the lower energy 34.1 eV from W 4f7/2, 36.5 eV from W 4f5/2 peaks are originated from reduced W<sup>5+</sup>. This result suggests that part of W atoms have been reduced to lower valence state. For 40CNCWO sample, O 1s binding-energy (BE) peaks are located at 533.1, 531.6 and 529.9 eV, (Fig. 4c), respectively, demonstrating the peak of 531.6 eV was corresponding to oxygen vacancies, which agrees with the reported BE values of O species [36]. The peak 529.9 eV and the peak 533.1 eV were corresponding to bond of O–W and O–H (H<sub>2</sub>O) respectively. And the chemical composition analysis based on the XPS (Tab. S1) indicated that the Cs/W atomic ratio is 0.326, which is very close to the theoretical maximum of 0.33. In addition, the concentration of oxygen vacancy in Cs<sub>0.326</sub>WO<sub>3</sub> equals 0.0543 mol/mol [37]. To further confirm the existence of oxygen vacancies, EPR experiments were employed, which can indicate the existence of at least one unpaired electron or singly ionized oxygen vacancies. There is a significant EPR signal at *g* = 2.006 observed which is originated by the trapped electrons in the oxygen vacancies (Fig. 4d). It is possible that the rich oxygen vacancies can be attributed to the formation of numerous W<sup>5+</sup> ions [20,38]. Besides, Because of the relatively rich W<sup>5+</sup> ions and oxygen vacancies, g-C<sub>3</sub>N<sub>4</sub>@Cs<sub>x</sub>WO<sub>3</sub> nanocomposites displayed outstanding optical properties.

The transmittance spectra of the as-prepared films are shown in Fig. 5a to display the optical transmittance spectra of the series of nanocomposites with the pure one for each component. All samples showed outstanding UV light isolating capability. Meanwhile, 10CNCWO, 40CNCWO and pure Cs<sub>x</sub>WO<sub>3</sub> demonstrated an average transmittance above 70% in the visible region (Fig. S3), respectively, which related to its wide band gap of Cs<sub>x</sub>WO<sub>3</sub>. Furthermore, series of nanocomposites and pure Cs<sub>x</sub>WO<sub>3</sub> demonstrated nice NIR absorbing performance, which can be further analyzed in the following mechanism sections.



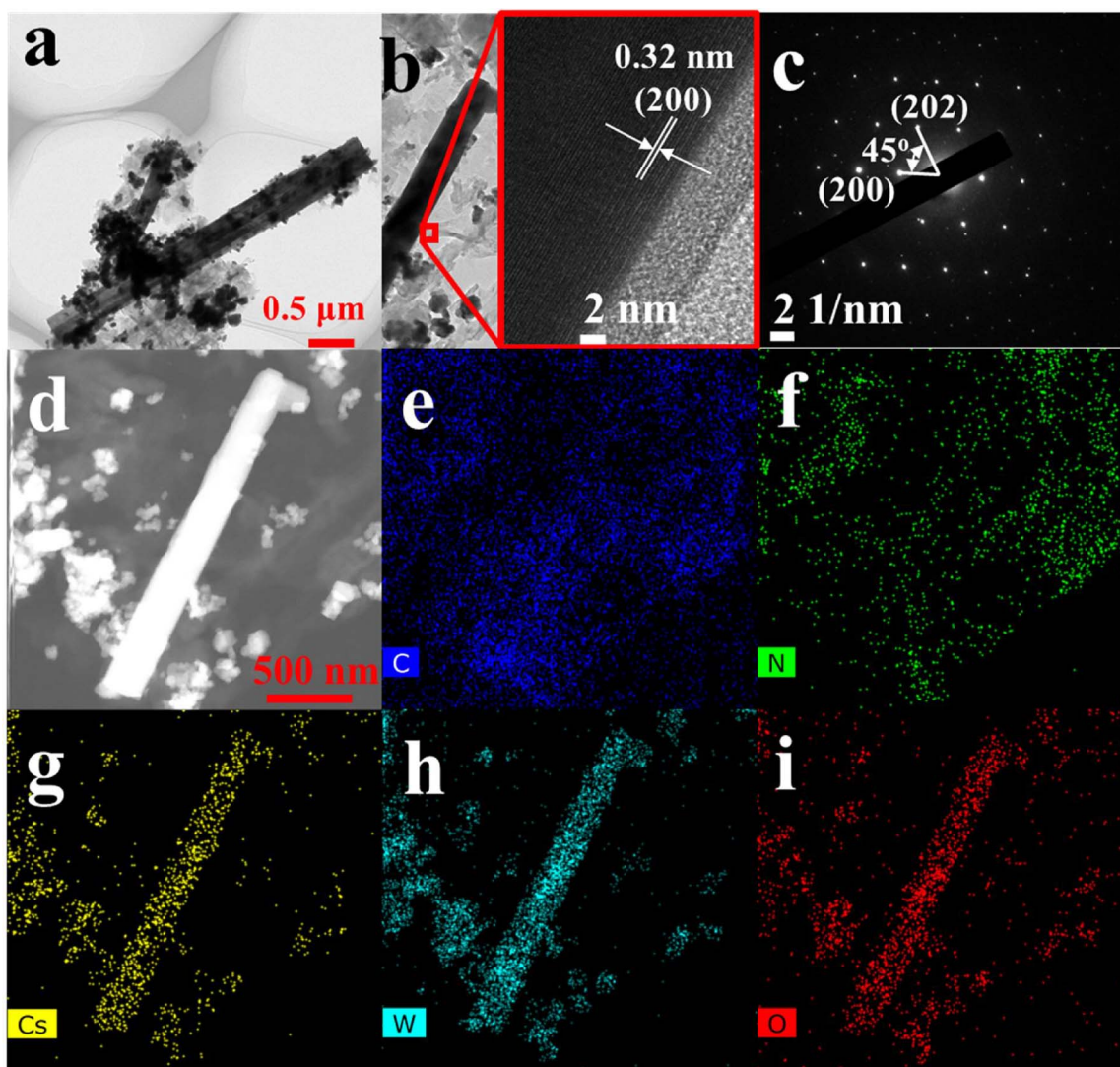


Fig. 3. TEM image of 40CNCWO (a), HRTEM image for 40CNCWO (b), SAED image for 40CNCWO (c), TEM image for 40CNCWO (d) and the representative element mapping images of 40CNCWO with the same scale bar of 500 nm, respectively (e–i).

Based on the above optical properties of CNCWO nanocomposites films, it is obviously believed that the series films can effectively absorb heat. Hence, the thermal insulation experiment has been carried out in an insulation-box (Fig. 5b) with the same background temperature. Fig. 5c exhibits the inner temperature variation via irradiation by 300 W Xe lamp for certain time. The temperature increases instantly with increasing irradiation time when the box is covered with no-coating quartz glass, which verifies that the quartz has no NIR shielding capacity. The heating rates of 40CNCWO coating is the lowest among of the no-coating quartz glass and ITO coating. Besides, the cooling temperature variation curves (Fig. 5d) show completely opposite tendency with the same start temperature (approximately 45 °C) and background temperature (approximately 28 °C). It is obviously that 40CNCWO film shows the best thermal insulation ability than others.

Moreover, the degradation of HCHO was carried out under the irradiation by various wavelength light respectively to test the photocatalytic activities of 40CNCWO. As seen in Fig. 6a, we can find out that, firstly, UV is the main energy source for the photodecomposition of HCHO. Secondly, such material also demonstrates interesting property to decompose the target gas under NIR irradiation with methanol as last products (Fig. 6e). Thirdly, it is easily to find out that only few Vis light is utilized by 40CNCWO for HCHO removal, hinting that most of Vis light penetrate this material. Besides, Fig. 6b shows the photodegradation of HCHO by different

samples under full spectrum lighting, respectively, illustrating that formaldehyde removal ability sequence is 70CNCWO > 100CNCWO > 140CNCWO > 40CNCWO > g-C<sub>3</sub>N<sub>4</sub> > 10CNCWO > Cs<sub>x</sub>WO<sub>3</sub>. However, the optical character of 70CNCWO, 100CNCWO and 140CNCWO are not suitable for window coating because of the bad Vis transmittance. Based on the Vis transmittance property and photocatalytic activity, the 40CNCWO has been selected as research target. The formaldehyde removal reactions are illustrated as following:



In addition, the insert Fig. 6c displays the catalytic performance of 40CNCWO for toluene removal under the irradiation by full spectrum lighting, demonstrating that toluene concentration approximately decreases 200 ppm under full spectrum irrigation during 240 min. Simultaneously, the CO<sub>2</sub> concentration approximately increases 420 ppm. The phenomenon of unmatched decrement of toluene and increment of CO<sub>2</sub> is possibly caused by either re-liquidation at the room temperature or incompletely decomposition. The inset of Fig. 6d, however, shows the corresponding GS-MS data for before toluene degradation and after

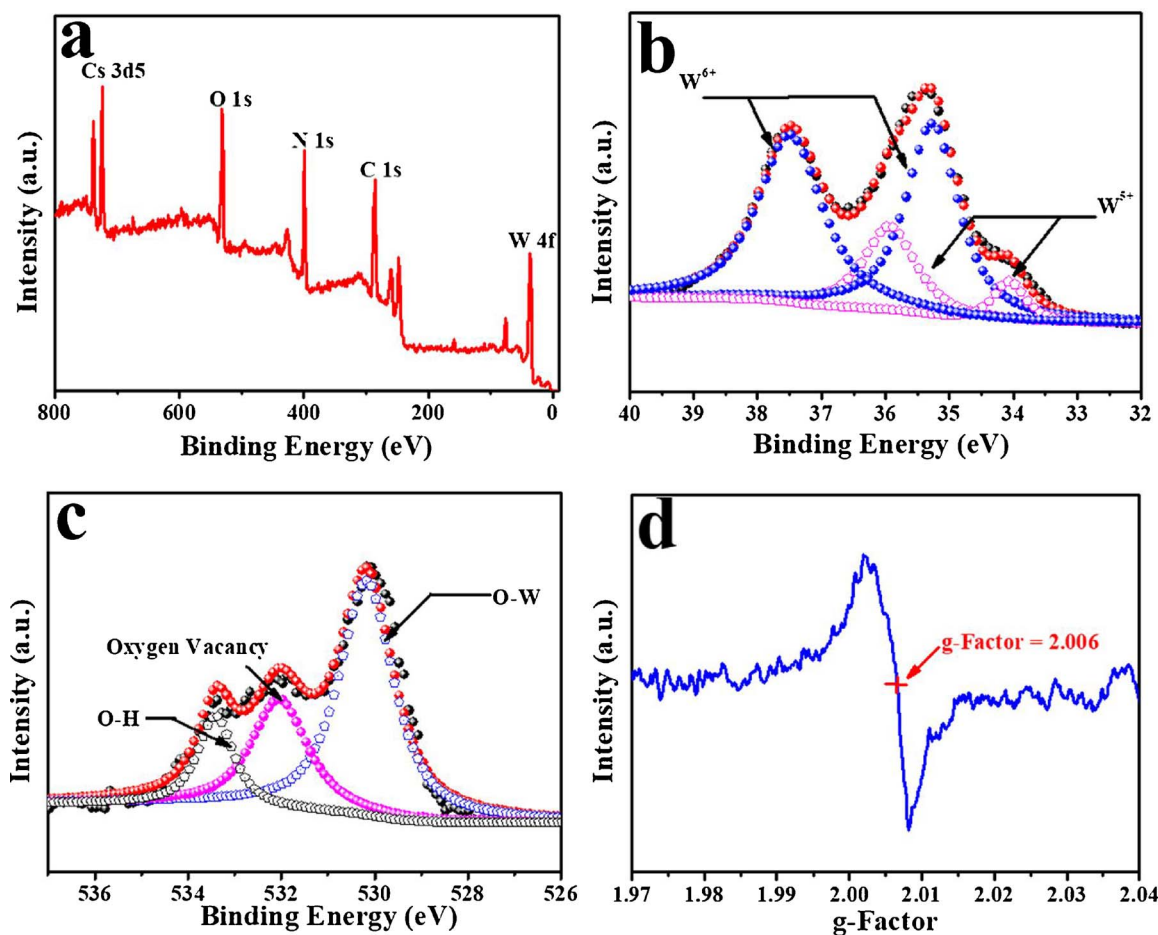


Fig. 4. Chemical composition and element valent of the as-prepared sample: survey spectrum (a), XPS spectra of W4f spectra (b), XPS spectra of O 1s spectra (c) and EPR spectra (d) of 40CNCWO.

toluene degradation, respectively, suggesting that no benzene derivative was generated as intermediary products during the degradation process, implying that the aromatic ring was cut off completely by certain oxidants. Meanwhile, the concentration of ethanol was decreasing during the toluene removal experiment (Fig. S4). The above data verify that the toluene should be decomposed completely.

The durability of the catalyst is of great significance for its practical applications. Fig. 6f reveals the cycling test of 40CNCWO in the process of HCHO photodegradation at 25 °C. Compared to that obtained in the first run, the HCHO removal ratio did not have significant change after 4 times repeat cycles, and slight fluctuating data of CO<sub>2</sub> possibly caused by the background concentration and the measurement deviation of device, suggesting that catalyst has excellent stability, because the Cs<sub>2</sub>WO<sub>3</sub> was protected by chemical/thermal-stable g-C<sub>3</sub>N<sub>4</sub>. To further verify this kind of smart window coating in practical applications, a piece of normal window pane has been used as light filter in the following test to simulate the reality scenario. The Fig. S5 illustrated that compared to the obtained data in the laboratory scenario, the HCHO removal ratio has not significant attenuation in the simulation scenario.

It is interesting that the series of CNCWO nanocomposites display nice photocatalytic ability. Therefore, radical species ( $\cdot\text{OH}$ ,  $\cdot\text{O}_2^-$ ,  $e^-$  and  $h^+$ ) trapping experiments were carried out to investigate the photocatalysis mechanism of the CNCWO composites for the degradation of HCHO. In the radical species trapping experiments, the same dosage (0.2 mmol) of potassium bichromate (injecting Ar for 20 min to remove O<sub>2</sub>), para-Quinone (BQ), salicylic acid and sodium oxalate were used as the scavengers of  $e^-$ ,  $\cdot\text{O}_2^-$ ,  $\cdot\text{OH}$  and  $h^+$ , respectively to investigate the active species in photocatalytic reaction. Fig. 7 shows the degradation ratio of HCHO over the 40CNCWO in the presence of

different scavengers. The adding potassium bichromate and BQ significantly impact on the photocatalytic activity of the composites, suggesting the  $\cdot\text{O}_2^-$  should be the mainly active reactant in the photocatalysis process. Especially, the increment of CO<sub>2</sub> takes on added importance in the adding BQ group, indicating that BQ preferentially react with  $\cdot\text{O}_2^-$  and produce more CO<sub>2</sub> than other groups. In the adding potassium bichromate group, the potassium bichromate was reduced by photogenerated electrons directly because of anaerobic environment. So, the concentration of HCHO decreased slowly as well because of the lacking of  $\cdot\text{O}_2^-$ . Meanwhile, compared to the no scavenger group, the decrement of HCHO and the increment of CO<sub>2</sub> in both of salicylic acid group and sodium oxalate group displayed insignificant change, which possibly hints that the  $h^+$  and  $\cdot\text{OH}$  don't effectively participate the process of HCHO removal due to some reasons.

To further make sure that g-C<sub>3</sub>N<sub>4</sub>@Cs<sub>2</sub>WO<sub>3</sub> could improve the photogenerated charge separation and electron transfer process, the photoelectrochemical measurements have been carried out. The transient photocurrent responses of g-C<sub>3</sub>N<sub>4</sub>@Cs<sub>2</sub>WO<sub>3</sub> composites and the pure one for each component (Fig. 8a) illustrate uniform photocurrent response in the as-prepared samples once the light-on and light-off. Compared to pure Cs<sub>2</sub>WO<sub>3</sub> and g-C<sub>3</sub>N<sub>4</sub>, 40CNCWO shows the best photocurrent response, which is about 1.2 times higher than that of g-C<sub>3</sub>N<sub>4</sub>. Based on that, it reveals that the photoinduced charge carriers in the 40CNCWO composite are separated efficiently than pure g-C<sub>3</sub>N<sub>4</sub> and Cs<sub>2</sub>WO<sub>3</sub>. Moreover, 40CNCWO still generates fewer current under NIR irradiation (Fig. 8b), which can be explained in the following mechanism sections in detail. In addition, 40CNCWO displayed the lowest electrical impedance among the three samples (Fig. 8c), verifying that 40CNCWO possibly possesses more free electrons inside.

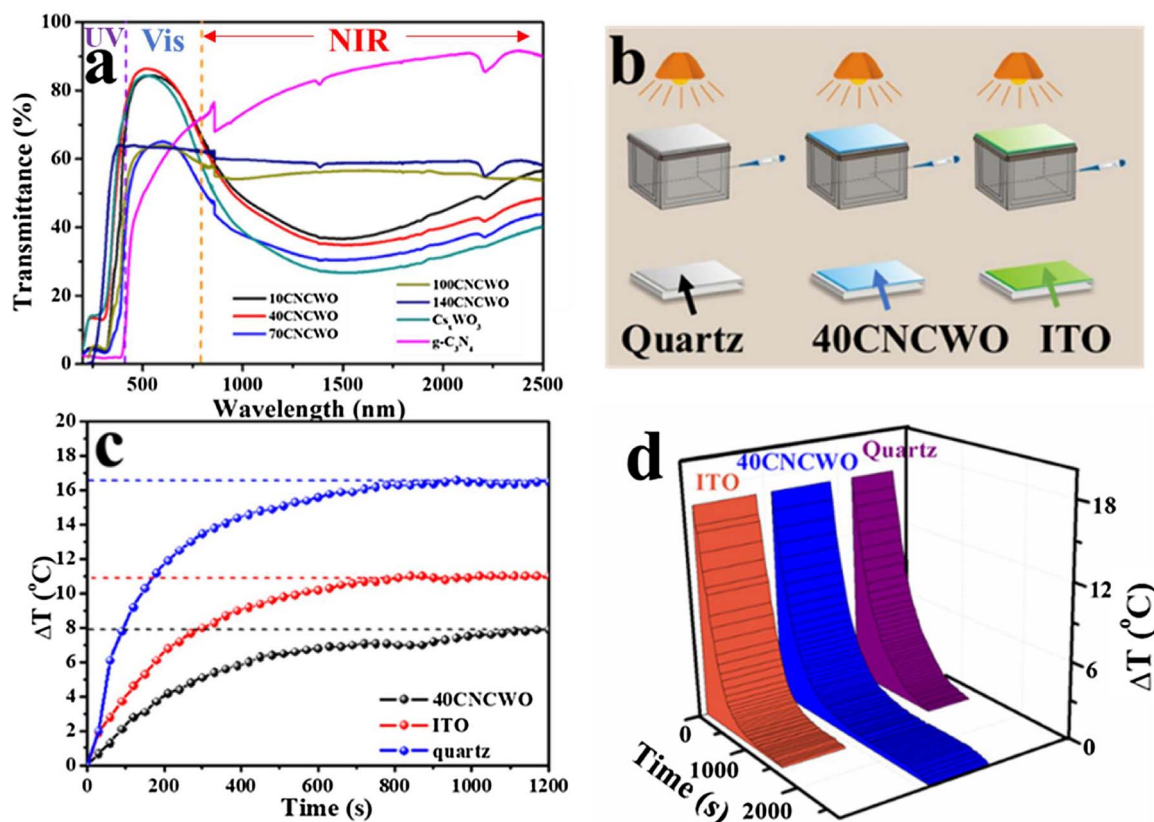


Fig. 5. Optical properties of CNCWO: Transmittance spectra of the films of 10CNCWO, 40CNCWO, 70CNCWO, 100CNCWO, 140CNCWO, pure  $\text{Cs}_x\text{WO}_3$  and  $\text{g-C}_3\text{N}_4$  (a), Schematic illustration of the thermal insulation simulated experiment (b), the inner heating temperature curves variation via irradiation by 300W Xe lamp (c) and the cooling temperature variation curves without extra heat resource (d).

Furthermore, the photoluminescence spectra were used to evaluate the ability of charge transition and separation. As shown in Fig. 8d, a broad and strong photoluminescence present at about 460 nm, which is attributed to the recombination process of self-trapped excitation [39]. For  $\text{g-C}_3\text{N}_4$ , the overlapped layers structure goes against the separation

of electrons and holes, which would lead to the strong PL emission [40,41]. For  $\text{C}_3\text{N}_4/\text{Cs}_x\text{WO}_3$ , the weaker luminescence suggests the lower recombination probability because Fig. S6a shows that pure  $\text{Cs}_x\text{WO}_3$  can not be formed upon excitation with UV light [42]. Therefore, the above PL and photoelectrochemical results suggest that

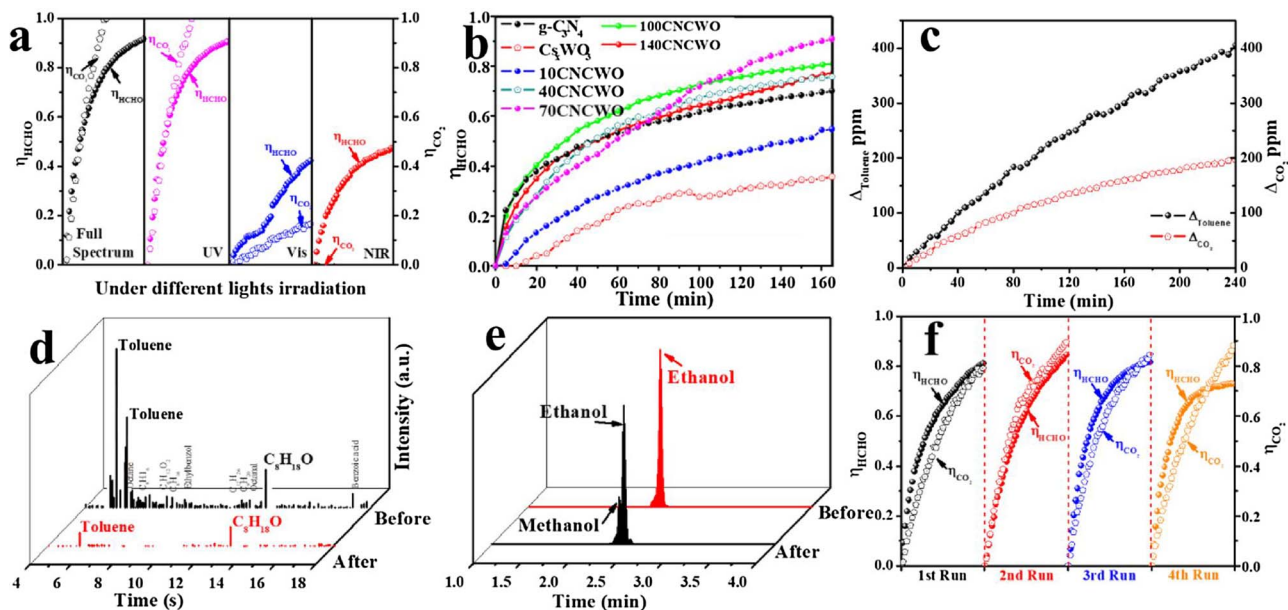


Fig. 6. Photocatalytic activities of as-prepared samples: the HCHO photodegradation under different wavelength light irradiation (a), the HCHO photodegradation for 10CNCWO, 40CNCWO, 70CNCWO, 100CNCWO, 140CNCWO, pure  $\text{Cs}_x\text{WO}_3$  and  $\text{g-C}_3\text{N}_4$  under full spectrum irradiation (b), the toluene photodegradation for 40CNCWO (c) and GC-MS data of before and toluene removal for 40CNCWO under full spectra irradiation (d), GC-FIT of before and HCHO removal for 40CNCWO under NIR light irradiation (e), the cycling test of 40CNCWO in the process of HCHO photodegradation at 25  $^{\circ}\text{C}$  (f).



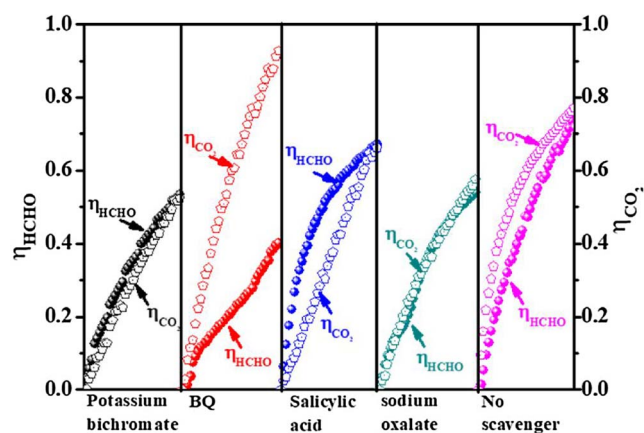


Fig. 7. Trapping experiments of active species during the photocatalytic degradation of HCHO for 40CNCWO.

$g\text{-C}_3\text{N}_4/\text{Cs}_x\text{WO}_3$  has highly efficient separation of photoinduced electrons and holes, which will be explained in the closing mechanism section in detail.

Obviously, the as-synthesized  $g\text{-C}_3\text{N}_4/\text{Cs}_x\text{WO}_3$  series displayed excellent PCO ability under UV light irradiation. HCHO and toluene were used as target contaminants to study the photocatalytic mechanism of  $g\text{-C}_3\text{N}_4/\text{Cs}_x\text{WO}_3$ . According to the result of the radical species trapping experiments, the photogenerated holes possibly annihilate or recombine with the rich free electron. Furthermore, as we know that the redox potential of  $\text{O}_2/\cdot\text{O}_2^-$  (-0.33 eV) is more positive than the CB of  $\text{Cs}_x\text{WO}_3$  (0.69 eV). So,  $\cdot\text{O}_2^-$  should be synthesized by  $\text{O}_2$

in the air and excited electrons from CB of  $g\text{-C}_3\text{N}_4$  (-1.01 eV). When we artificially set up an oxygen-deficient atmosphere in the degradation experiment or add other reactants which can preferentially react with  $\cdot\text{O}_2^-$ , the PCO process of  $g\text{-C}_3\text{N}_4/\text{Cs}_x\text{WO}_3$  nanocomposites will be restrained. More importantly, the oxygen chemisorption enhanced at oxygen vacancies. The photogenerated electrons can easily transfer to chemisorbed  $\text{O}_2$  molecular and generated  $\cdot\text{O}_2^-$  [43]. Overall,  $\cdot\text{O}_2^-$  is the mainly active specie in the PCO process which correspond to the resulting of radical species trapping experiments. Hence, the whole process of PCO is following (Fig. 9) that when the  $g\text{-C}_3\text{N}_4/\text{Cs}_x\text{WO}_3$  nanocomposites are irradiated by UV light, the photogenerated hole in the VB of  $\text{C}_3\text{N}_4$  will recombine with the photogenerated electron in the CB of  $\text{Cs}_x\text{WO}_3$ , which is beneficial for separation of photoinduced hole-electron pairs, which correspond to the results of photoelectrochemical and PL measurements. Obviously, a typical Z-scheme heterostructure can be formed between  $\text{Cs}_x\text{WO}_3$  and  $g\text{-C}_3\text{N}_4$  in composite. The Z-scheme heterostructure of nanocomposites can effectively exploit the energy of UV light in the PCO process.

As shown in Fig. 9, the NIR-catalysis highly relate to localized electrons hopping [44–46]. Cs ions with larger ionic radius occupy the center of HC and donate outer-d valence electrons to the empty sites of  $\text{W}^{5+}$  5d orbits with higher activity energy. Meanwhile, oxygen vacancies in the crystal of  $\text{Cs}_x\text{WO}_3$  also supply extra free electrons. Both of above free electrons can be localized (small polarons) which just below the CB of  $\text{WO}_3$  [47]. Accordingly, the short wavelengths of NIR spectrum (730–1100 nm) can trigger the small polarons to jump to CB and generate corresponding NIR photocurrent [48]. Then, the excited free electrons promptly transfer to the surface of materials and reduce HCHO to low-toxic methanol [49]. The chemical reactions are

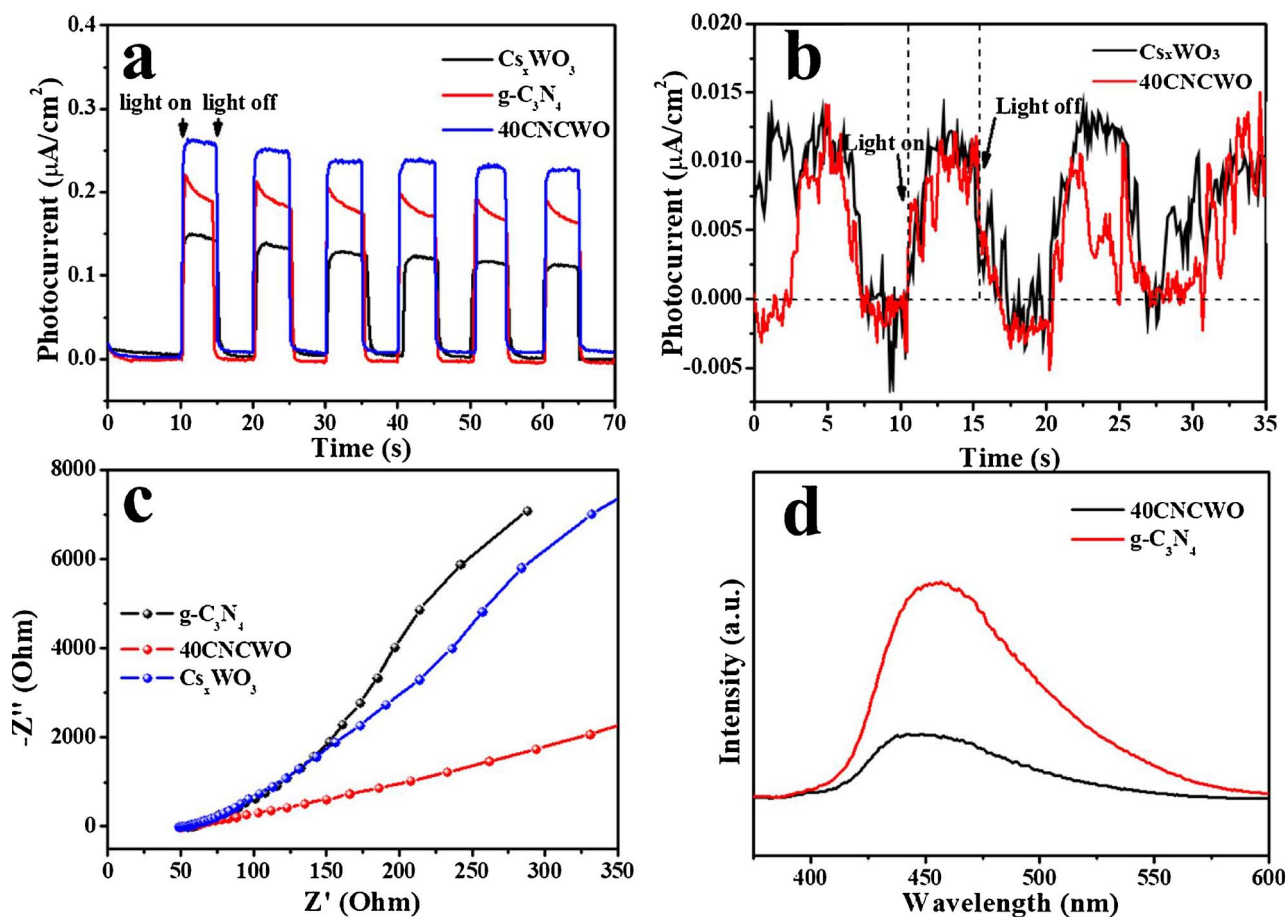


Fig. 8. Photoelectrochemical current for 40CNCWO, pure  $\text{Cs}_x\text{WO}_3$  and  $g\text{-C}_3\text{N}_4$  under full spectrum irradiation (a), pure  $\text{Cs}_x\text{WO}_3$  and 40CNCWO under NIR irradiation (b), respectively, electrical impedance curves for 40CNCWO, pure  $\text{Cs}_x\text{WO}_3$  and  $g\text{-C}_3\text{N}_4$  (c), and photoluminescence spectrum for 40CNCWO and  $g\text{-C}_3\text{N}_4$  (d).

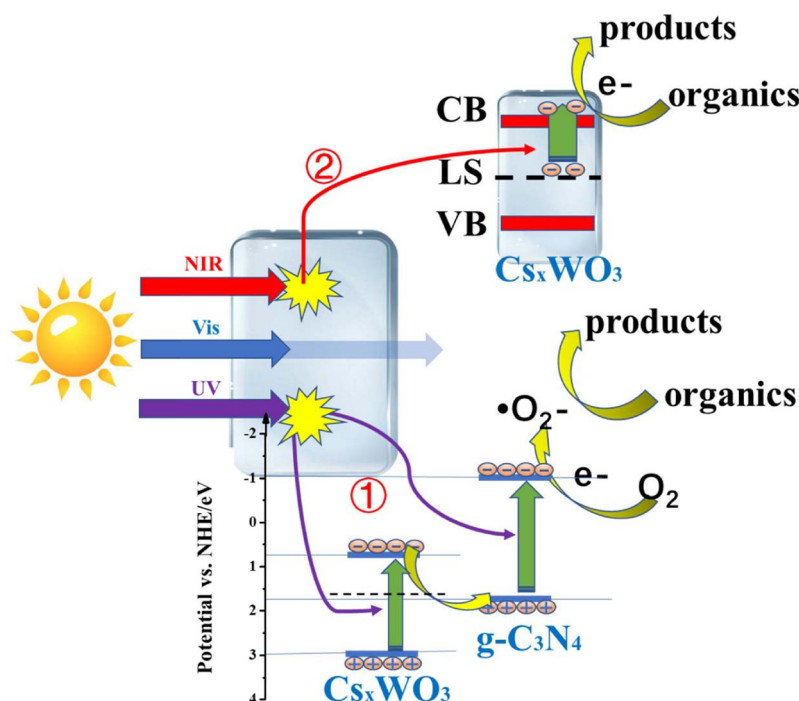


Fig. 9. Detail for the multifunctional properties of Z-scheme  $g\text{-C}_3\text{N}_4@\text{Cs}_x\text{WO}_3$  heterostructure.

illustrated as following:



#### 4. Conclusions

We have successfully synthesized the  $g\text{-C}_3\text{N}_4@\text{Cs}_x\text{WO}_3$  nanocomposites which not only displayed strong absorption of harmful UV/NIR light as well as high transparency for visible light, but also demonstrated nice photocatalytic depollution ability. The radical species ( $\cdot\text{OH}$ ,  $\cdot\text{O}_2^-$ ,  $e^-$  and  $h^+$ ) trapping experiments revealed that a typical Z-scheme heterostructure was formed between  $\text{Cs}_x\text{WO}_3$  and  $g\text{-C}_3\text{N}_4$  in composite. In addition, both of photoelectrochemical measurements and photoluminescence spectra verified that UV light induced Z-scheme heterostructure highly enhance the separated of charge carriers and promote PCO ability. Besides, electrical impedance curves validated that rich free electrons existed in the  $g\text{-C}_3\text{N}_4@\text{Cs}_x\text{WO}_3$ . The free electrons easily jumped to CB as form of small polarons and generated correspondent photocurrent under short wavelength of NIR light (730–1100 nm) irradiation, which has been confirmed by NIR photoelectrochemical measurements. In addition, the aggregated free electrons in the CB generated the localized surface plasma resonance (LSPR) to shield the same oscillation frequency of NIR light (1100–2500 nm). The above NIR light shielding processes have been proved by the transmittance spectra of  $g\text{-C}_3\text{N}_4@\text{Cs}_x\text{WO}_3$  nanocomposites. Based on the above mechanisms and the removal results in the simulation scenario, as synthesized  $g\text{-C}_3\text{N}_4@\text{Cs}_x\text{WO}_3$  nanocomposites are highly suitable for practical application as smart window coating. This work provided novel thought into the synthesis of the environmental friendly materials as smart window coating.

#### Acknowledgments

This work was supported by the National Natural Science Foundation of China (NSFC No. 51472194 and No. 51602237), the

Fundamental Research Funds for the Central Universities (WUT:2017 IVA 039 and 2017 IVB 015) and the National Basic Research Program of China (973 Program No. 2013CB632402).

#### Appendix A. Supplementary data

The SI contains the schematic of photocatalytic test system, photograph of 40CNCWO coating and photocatalytic activities of samples.

Supplementary material related to this article can be found, in the online version, at doi:<https://doi.org/10.1016/j.apcatb.2018.02.024>.

#### References

- [1] WHO guidelines for indoor air quality: selected pollutants, World Health Organization 291 Regional Office for Europe: Copenhagen, Denmark, 2010.
- [2] J.W. Ye, X.F. Zhu, B. Cheng, J.G. Yu, C.J. Jiang, Few-layered graphene-like Boron nitride: a highly efficient adsorbent for indoor formaldehyde removal, *Environ. Sci. Technol. Lett.* 49 (2017) 20–25.
- [3] C. Bechinger, S. Ferrere, A. Zaban, J. Sprague, B. Gregg, Photoelectrochromic windows and displays, *Nature* 383 (1996) 608–610.
- [4] C.G. Granqvist, A. Azensb, P. Heszler, L.B. Kishd, L. Osterlunde, Nanomaterials for benign indoor environments: electrochromics for “smart windows”, sensors for air quality, and photo-catalysts for air cleaning, *Sol. Energ. Mat. Sol. C* 91 (2007) 355–365.
- [5] M. Kanehara, H. Koike, T. Yoshinaga, T. Teranishi, Indium tin oxide nanoparticles with compositionally tunable surface plasmon resonance frequencies in the near-IR region, *J. Am. Chem. Soc.* 131 (2009) 17736–17737.
- [6] V. Senthilkumar, P. Vickraman, M. Jayachandran, C. Sanjeeviraja, Structural and optical properties of indium tin oxide (ITO) thin films with different compositions prepared by electron beam evaporation, *Vacuum* 84 (2010) 864–869.
- [7] P. Pattathil, R. Giannuzzi, M. Manca, Self-powered NIR-selective dynamic windows based on broad tuning of the localized surface plasmon resonance in mesoporous ITO electrodes, *Nano Energy* 30 (2016) 242–251.
- [8] M.M. Qazilbash, M. Brehm, B.G. Chae, P.C. Ho, G.O. Andreev, B.J. Kim, S.J. Yun, A.V. Balatsky, M.B. Maple, F. Keilmann, Mott transition in  $\text{VO}_2$  revealed by infrared spectroscopy and nano-imaging, *Science* 318 (2007) 1750–1753.
- [9] Z.T. Zhang, Y.F. Gao, Z. Chen, J. Du, C.X. Cao, L.T. Kang, H.J. Luo, Thermochromic  $\text{VO}_2$  thin films: solution-based processing, improved optical properties, and lowered phase transformation temperature, *Langmuir* 26 (2010) 10738–10744.
- [10] S. Bonora, U. Bortolozzo, S. Residori, R. Balu, P.V. Ashrit, Mid-IR to near-IR image conversion by thermally induced optical switching in vanadium dioxide, *Opt. Lett.* 35 (2010) 103–105.
- [11] L.S. Long, H. Ye, Dual-intelligent windows regulating both solar and long-wave radiations dynamically, *Sol. Energ. Mat. Sol. C* 169 (2017) 145–150.
- [12] K. Adachi, M. Miratsu, T. Asahi, Absorption and scattering of near-infrared light by



- dispersed lanthanum hexaboride nanoparticles for solar control filters, *J. Mater. Res.* 25 (2010) 510–521.
- [13] C.J. Chen, D.H. Chen, Preparation of  $\text{LaB}_6$  nanoparticles as a novel and effective near-infrared photothermal conversion material, *Chem. Eng. J.* 180 (2012) 337–342.
- [14] E. Sani, L. Mercatelli, M. Meucci, L. Zoli, D. Sciti, Lanthanum hexaboride for solar energy applications, *Sci. Rep.* 7 (2017), <http://dx.doi.org/10.1038/s41598-017-00749-w>.
- [15] H. Takeda, K. Adachi, Near infrared absorption of tungsten oxide nanoparticle dispersions, *J. Am. Ceram. Soc.* 90 (2007) 4059–4061.
- [16] C.S. Guo, S. Yin, Y.F. Huang, Q. Dong, T. Sato, Synthesis of  $\text{W}_{18}\text{O}_{49}$  Nanorod via ammonium tungsten oxide and its interesting optical properties, *Langmuir* 27 (2011) 12172–12178.
- [17] Z. Chen, Y.T. Peng, F. Liu, Z.Y. Le, J. Zhu, G.R. Shen, D.Q. Zhang, M.C. Wen, S.N. Xiao, C.P. Liu, Y.F. Lu, H.X. Li, Hierarchical nanostructured  $\text{WO}_3$  with bio-mimetic proton channels and mixed ionic-electronic conductivity for electro-chemical energy storage, *Nano Lett.* 15 (2015) 6802–6808.
- [18] X.Y. Wu, S. Yin, D.F. Xue, S. Komarneni, T. Sato, A  $\text{Cs}_x\text{WO}_3/\text{ZnO}$  nanocomposite as a smart coating for photocatalytic environmental cleanup and heat insulation, *Nanoscale* 7 (2015) 17048–17054.
- [19] X.Y. Wu, J.T. Wang, G.K. Zhang, K. Katsumata, K. Yanagisawa, T. Sato, S. Yin, Series of  $\text{M}_x\text{WO}_3/\text{ZnO}$  ( $\text{M} = \text{K}, \text{Rb}, \text{NH}_4$ ) nanocomposites: combination of energy saving and environmental decontamination functions, *Appl. Catal. B* 201 (2017) 128–136.
- [20] K. Kenji Adachia, T. Asahji, Activation of plasmons and polarons in solar control cesium tungsten bronze and reduced tungsten oxide nanoparticles, *J. Mater. Res.* 27 (2012) 965–970.
- [21] C.X. Yang, J.F. Chen, X.F. Zeng, D.J. Cheng, D.P. Cao, Design of the alkali-metal-doped  $\text{WO}_3$  as a near-infrared shielding material for smart window, *Ind. Eng. Chem. Res.* 53 (2014) 17981–17988.
- [22] L.Y. Li, F. Jiang, F.F. Tu, S.F. Jia, Y.H. Gao, J.B. Wang, Atomic-scale study of cation ordering in potassium tungsten bronze nanosheets, *Adv. Sci.* (2017), <http://dx.doi.org/10.1002/advs.201600537>.
- [23] G.V. Naik, V.M. Shalae, A. Boltasseva, Alternative plasmonic materials: beyond gold and silver, *Adv. Mater.* 25 (2013) 3264–3294.
- [24] W.L. Yu, J.X. Chen, T.T. Shang, L.F. Chen, L. Gu, T.Y. Peng, Direct Z-scheme  $\text{g-C}_3\text{N}_4/\text{WO}_3$  photocatalyst with atomically defined junction for  $\text{H}_2$  production, *Appl. Catal., B* 219 (2017) 693–704.
- [25] K. Wang, G.K. Zhang, J. Li, Y. Li, X.Y. Wu, 0D/2D Z-scheme heterojunctions of bismuth tantalate quantum dots/ultrathin  $\text{g-C}_3\text{N}_4$  nanosheets for highly efficient visible light photocatalytic degradation of antibiotics, *ACS. Appl. Mater. Interfaces* 9 (2017) 43704–43715.
- [26] J.S. Zhang, M.W. Zhang, L.H. Lin, X.C. Wang, Sol processing of conjugated carbon nitride powders for thin-film fabrication, *Angew. Chem. Int. Ed.* 54 (2015) 1–6.
- [27] J. Xu, L.W. Zhang, R. Shi, Y.F. Zhu, Chemical exfoliation of graphitic carbon nitride for efficient heterogeneous photocatalysis, *J. Mater. Chem. A* 46 (2013) 14766–14772.
- [28] S.W. Cao, J.X. Low, J.G. Yu, M. Jaroniec, Polymeric photocatalysts based on graphitic carbon nitride, *Adv. Mater.* 27 (2015) 2150–2176.
- [29] J. Xu, Z.P. Wang, Y.F. Zhu, Enhanced visible-light-driven photocatalytic disinfection performance and organic pollutant degradation activity of porous  $\text{g-C}_3\text{N}_4$  nanosheets, *ACS. Appl. Mater. Inter.* 33 (2017) 27727–27735.
- [30] J. Wang, Z. Yang, X.X. Gao, W.Q. Yao, W.Q. Wei, X.J. Chen, R.L. Zong, Y.F. Zhu, Core-shell  $\text{g-C}_3\text{N}_4/\text{ZnO}$  composites as photoanodes with double synergistic effects for enhanced visible-light photoelectrocatalytic activities, *Appl. Catal. B* 217 (2017) 169–180.
- [31] C.S. Pan, J. Xu, Y.J. Wang, D. Li, Y.F. Zhu, Dramatic activity of  $\text{C}_3\text{N}_4/\text{BiPO}_4$  photocatalyst with core/shell structure formed by self-assembly, *Adv. Funct. Mater.* 22 (2012) 1518–1524.
- [32] C.S. Guo, S. Yin, M. Yan, T. Sato, Facile synthesis of homogeneous  $\text{Cs}_x\text{WO}_3$  nanorods with excellent low-emissivity and NIR shielding property by a water controlled-release process, *J. Mater. Chem.* 21 (2011) 5099–5105.
- [33] Q.Y. Lin, L. Li, S.J. Liang, M.H. Liu, J.H. Bi, L. Wu, Efficient synthesis of monolayer carbon nitride 2D nanosheet with tunable concentration and enhanced visible-light photocatalytic activities, *Appl. Catal. B* 163 (2015) 135–142.
- [34] D. Ma, J. Wu, M.C. Gao, Y.J. Xin, T.J. Ma, Y.Y. Sun, Fabrication of Z-scheme  $\text{g-C}_3\text{N}_4/\text{RGO}/\text{Bi}_2\text{WO}_6$  photocatalyst with enhanced visible-light photocatalytic activity, *Chem. Eng. J.* 290 (2016) 136–146.
- [35] J. Tian, Y.H. Sang, G.W. Yu, H.D. Jiang, X.N. Mu, H. Liu, A  $\text{Bi}_2\text{WO}_6$ -based hybrid photocatalyst with broad spectrum photocatalytic properties under UV, visible, and near-infrared irradiation, *Adv. Mater.* 25 (2013) 5075–5080.
- [36] Y.F. Sun, S. Gao, F.C. Lei, Y. Xie, Atomically-thin two-dimensional sheets for understanding active sites in catalysis, *Chem. Soc. Rev.* 44 (2015) 623–636.
- [37] G.L. Li, C.S. Guo, M. Y, S.Q. Liu,  $\text{Cs}_x\text{WO}_3$  nanorods: realization of full-spectrum-responsive photocatalytic activities from UV, visible to near-infrared region, *Appl. Catal. B* 183 (2016) 142–148.
- [38] L.S. Cavalcante, V.M. Longo, M. Zampieri, J.W.M. Espinosa, P.S. Pizani, J.R. Sambrano, J.A. Varela, E. Longo, M.L. Simões, C.A. Paskocimas, Experimental and theoretical correlation of very intense visible green photoluminescence in  $\text{BaZrO}_3$  powders, *J. Appl. Phys.* 103 (2008) 063527–063535.
- [39] S. Tretiak, A. Saxena, R.L. Martin, A.R. Bishop, Conformational dynamics of photoexcited conjugated molecules, *Phys. Rev. Lett.* 89 (2002) 097402.
- [40] X.Y. Wu, M.M. Li, J. Li, G.K. Zhang, S. Yin, A sillenite-type  $\text{Bi}_{12}\text{MnO}_{20}$  photocatalyst: UV, visible and infrared lights responsive photocatalytic properties induced by the hybridization of Mn 3d and O 2p orbitals, *Appl. Catal. B* 219 (2017) 132–141.
- [41] A.D. Yoffe, Semiconductor quantum dots and related systems: electronic, optical, luminescence and related properties of low dimensional systems, *Adv. Phys.* 50 (2001) 1–208.
- [42] K.S. Lee, D.K. Seo, M.H. Whangbo, Electronic band structure study of the anomalous electrical and superconducting properties of hexagonal alkali tungsten bronzes  $\text{A}_x\text{WO}_3$  ( $\text{A} = \text{K}, \text{Rb}, \text{Cs}$ ), *J. Am. Chem. Soc.* 119 (1997) 4043–4049.
- [43] N. Zhang, X.Y. Li, H.C. Ye, S.M. Chen, H.X. Ju, D.B. Liu, Y. Lin, W. Ye, C.M. Wang, Q. Xu, J.F. Zhu, L. Song, J. Jiang, Y.J. Xiong, Oxide defect engineering enables to couple solar energy into oxygen activation, *J. Am. Chem. Soc.* 138 (2016) 8928–8935.
- [44] D.B. Migas, V.L. Shaposhnikov, V.N. Rodin, V.E. Borisenko, Tungsten oxides. I. Effects of oxygen vacancies and doping on electronic and optical properties of different phases of  $\text{WO}_3$ , *J. Appl. Phys.* 108 (2010) 093713–093726.
- [45] T. Gao, P.J. Björn, Visible-light-driven photochromism of hexagonal sodium tungsten bronze nanorods, *J. Phys. Chem. C* 117 (2013) 13753–13761.
- [46] H.D. Zheng, J.Z. Ou, M.S. Strano, R.B. Kaner, A. Mitchell, K. Kalantar-zadeh, Nanostructured tungsten oxide-properties, synthesis, and applications, *Adv. Funct. Mater.* 21 (2011) 2175–2196.
- [47] K.S. Lee, D.K. Seo, M. Whangbo, Electronic band structure study of the anomalous electrical and superconducting properties of hexagonal alkali tungsten bronzes  $\text{A}_x\text{WO}_3$  ( $\text{A} = \text{K}, \text{Rb}, \text{Cs}$ ), *J. Am. Chem. Soc.* 119 (1997) 4043–4049.
- [48] J. Li, X.Y. Wu, W.F. Pan, G.K. Zhang, H. Chen, Vacancy-rich monolayer  $\text{BiO}_{2-x}$  as highly efficient UV, visible and near-infrared responsive photocatalyst, *Angew. Chem. Int. Ed.* 130 (2018) 500–504.
- [49] T. Inoue, A. Fujishima, S. Konishi, K. Honda, Photoelectrocatalytic reduction of carbon dioxide in aqueous suspensions of semiconductor powders, *Nature* 277 (1979) 637–638.